An Investigation of the Surface Pressure Fields beneath Simulated Tornado Cyclones

J. T. SNOW, C. R. CHURCH AND B. J. BARNHART[1]

Purdue University, West Lafayette, IN 47907

(Manuscript received 20 July 1979, in final form 21 December 1979)

ABSTRACT

The wall static pressure fields beneath tornado-like vortices have been investigated using a large vortex generator especially designed to model tornado cyclone airflow. Presented in nondimensional form, the data include both a series of radial profiles across the mean pressure field under a variety of flow conditions, and a detailed investigation of the magnitude of the central pressure as a function of swirl. The profiles clearly show the development of the intense vortical core from the no-swirl state, and the evolution of the core from a one-celled into a two-celled flow. For the experimental range examined, it is found that the greatest pressure deficits and largest pressure gradients (in the mean field) are associated with single-celled vortices. Strong evidence is found for the existence of a dynamically induced downdraft in the two-celled vortex.

1. Introduction

Occasionally, barograph traces are obtained in the near vicinity of tornadic events. Particularly good examples are to be found in Fujita (1959, 1970) and in Ward (1964). These traces represent one of the few sources of directly measured quantitative data concerning tornado cyclones. To obtain a better physical understanding of the mechanisms producing the surface pressure fields recorded on these barograph traces, a series of laboratory experiments has been carried out in a large vortex generator. The generator, modeled after that of Ward (1972), is especially designed to replicate the situation wherein tornado production is the result of radial convergence of angular momentum in a large-scale rotating updraft (mesocyclone). As shown in Fig. 1, the physical arrangement of the apparatus is such that geometric and dynamic similarity to a rotating updraft is attained (Davies-Jones, 1973, 1976). The model tornado cyclone forms in the central portion of a flat, disk-shaped volume (labeled the confluence and convergence regions in Fig. 1) at the base of this updraft. In this system, the tornado corresponds to the central core of the tornado cyclone. Detailed discussion of the physical basis for the modeling in the Ward-type tornado simulator is contained in Church *et al.* (1979).

2. Similarity parameters

In the similarity arguments contained in Lewellen (1962), Davies-Jones (1973, 1976) and Church *et al.* (1977, 1979), it is shown that for a fixed external geometry, the character of the flow in the confluence and convergence regions of the simulator is determined by three dimensionless internal parameters:

$$\text{Swirl parameter} = \Gamma/Q, \tag{1}$$

$$\text{Re}_r = \text{radial Reynolds number} = Q/\nu, \tag{2}$$

$$a = \text{internal aspect ratio of the convergence region} = h/r_0, \tag{3}$$

where Γ is the circulation input to the convergence region, Q the radial volume flow rate, per unit axial length, r_0 the radius of the updraft hole and h the depth of the confluence region. In the governing equations of motion, the swirl parameter and the aspect ratio appear in combination as

$$S = \text{swirl ratio} = \frac{r_0\Gamma}{2Qh}, \tag{4}$$

where the factor of 2 in the denominator has been incorporated following Davies-Jones (1973).

The swirl ratio describes the relative strength of the tangential velocity field compared to the flow-through field and has been shown by Davies-Jones (1973, 1976) to be the parameter which determines the core radius and the transitions to the multiple-vortex states. The radial Reynolds number gives a measure of the importance of dissipation in the boundary inflow layer. The internal aspect ratio fixes the geometry of the convergence region wherein the core of the model tornado cyclone develops. The values of these quantities likely to occur in nature and those obtainable in the Ward-

[1] Present affiliation: Analytic Services, Arlington, VA 22202.

0022-4928/80/051013-14$07.50

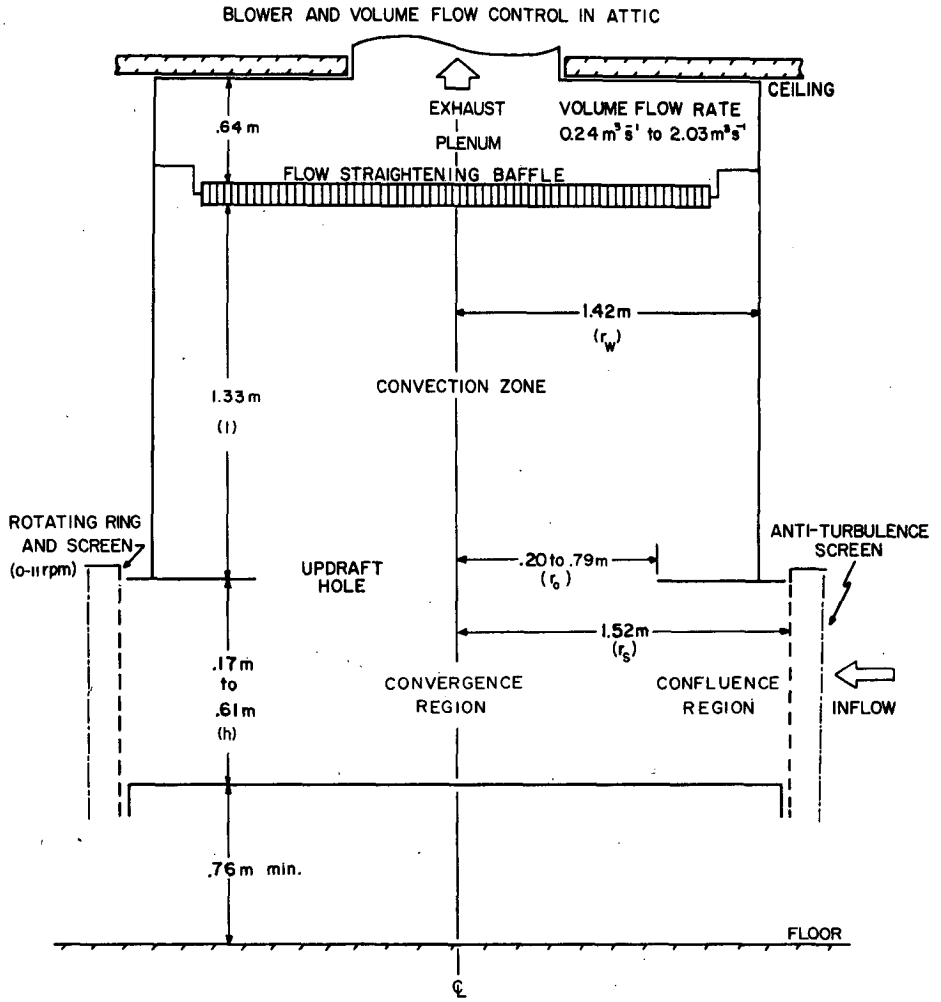

FIG. 1. Vertical cross-section schematic through the Purdue University tornado vortex simulator. Exhaust system and volume flow rate measuring assembly are located in the room above (not shown).

type generator used in the present work are given in Church *et al.* (1979).

3. Experimental procedures

To measure the wall static pressure deficit on the lower surface, two probes were made. Each probe consisted of a thin square brass plate with beveled edges. A small sensing orifice was drilled through the flat face of each plate, and a pressure tap centered on this hole and soldered to the underside. These probes were mounted flat on the lower surface, the pressure taps extending downward through the surface. One probe was fixed at large radius (~1.3 m) to provide a far-field reference value. The other probe could be moved radially across the lower surface by means of a positioning assembly affixed to the bottom side of that surface.

Each of the probes was connected to one side of a variable reluctance differential pressure transducer. With a full-scale output of 10 V dc for a 0.69 mb pressure difference across the input ports, this transducer was able to resolve differences as small as 7×10^{-4} mb. The output voltage of the transducer was passed through an adjustable time constant low-pass filter to remove high-frequency fluctuations, and was then read on a digital voltmeter. The transducer output was also observed directly using an oscilloscope.

In the first series of experiments, measurements were made of the time-mean value of wall static pressure deficit (with respect to the pressure at the fixed reference probe) on the lower surface of the convergence and confluence regions. Values were read successively at a number of positions along a portion of a diameter. The data points were adjusted, non-

dimensionalized, and then plotted to obtain a radial profile across the wall static pressure field on the lower surface. The measured data were adjusted for offset errors, but were not smoothed. Radial position was adjusted by subtracting out a radial offset due to the vortex centerline not coinciding with the centerline of the apparatus. This offset was determined by plotting each set of raw data, and then shifting the profile to force radial symmetry in the far field. A pressure difference offset due to drift in the electronics associated with the transducer was subtracted from the observed values of pressure difference. This pressure offset was determined by measuring the no-swirl pressure profile before and after each data run and noting the mean difference. In order to check our ability to replicate the results, in several cases two sets of data for the same flow conditions were taken. The period of time between two sets of observations ranged from several days to several weeks. Comparison of these repeated sets showed a high degree of repeatability in profile shape to include small-scale details.

A detailed qualitative examination of each vortex selected for investigation was accomplished by visualizing the flow with a kerosene fog. When injected into the boundary layer at large radius, this fog allowed the details of the surface inflow and of the central core to be discerned. This technique was particularly important in determining the radius at which boundary-layer separation occurred. Kerosene fog was also injected into the flow on the downstream (top) side of the flow straightening baffle. This fog was drawn downward by the downdrafts in the two-celled vortices and allowed the depth of penetration and the intensity of these downdrafts to be estimated.

To characterize each flow for which pressure data were taken, the four dimensionless internal parameters of Eqs. (1)–(4) were determined. The aspect ratio a was set by configuring the apparatus. The volume flow rate Qh was monitored continuously by use of a pitot rake assembly in the chamber exhaust system. The value of the swirl parameter was determined at the beginning of each experiment by measuring a representative inflow angle θ, where

$$\tan\theta = \Gamma/Q. \tag{5}$$

This measurement was made with a hot-film anemometer using the peaking procedure described in Church *et al.* (1979). The representative value for θ was taken to be its value at a radius of 1 m, at midheight between the top and bottom surfaces of the confluence zone. The single-film anemometer was also used to measure a few values of the magnitude of the total velocity vector at selected points within the flow to aid in interpreting the pressure traces.

A major source of difficulty in the pressure measurement program was the oscillations generated by vortex wander. This effect was most serious for vortical flows having small core regions, as these had the steepest pressure gradients at the edge of the core. As the vortex axis moved about the geometric centerline of the apparatus, the measurement system recorded the motion as an oscillation in the pressure. Because of this effect, the filtering process resulted in an underestimate of the actual minimum pressure deficit within the core. For the small cores, the vortex wander observed was about 10–15% of the core radius. For large, two-celled vortices the wander decreased to 1–2%.

4. Nondimensionalization

The data were nondimensionalized to facilitate identification of those parameters controlling the shapes of the profiles and the magnitudes of the central pressure drops. To arrive at an appropriate nondimensionalization scheme, a simple inviscid model for the flow next to the lower surface in the confluence and outer portion of the convergence zone was assumed, with

$$v_r = \begin{cases} -V_{r0}\left(\dfrac{r_0}{r}\right), & r_0 \leq r \qquad (6a) \\ -V_{r0}\left(\dfrac{r}{r_0}\right), & r_c < r \leq r_0 \qquad (6b) \end{cases}$$

$$v_\theta = V_{\theta 0}\left(\frac{r_0}{r}\right), \qquad r_c < r, \tag{7}$$

$$v_z = 0, \qquad r_c < r. \tag{8}$$

Here

$$V_{r0} = \text{characteristic radial velocity} = Q/2\pi r_0, \tag{9}$$

$$V_{\theta 0} = \text{characteristic tangential velocity} = \Gamma/2\pi r_0, \tag{10}$$

r_c = (unspecified) vortex core radius $\leq r_0$.

The characteristic velocities V_{r0} and $V_{\theta 0}$ are taken to be averages over the cylindrical wall of the convergence region ($r = r_0$, $0 < z \leq h$). While radial momentum is not conserved across the confluence zone ($r_0 \leq r \leq r_s$) due to the acceleration resulting from the forced convergence, radial mass flux and tangential angular momentum are conserved, so that the swirl parameter is constant in this region. No attempt was made to extend the simple model into the core zone ($r \leq r_c$) as this flow was found to be highly complex.

Using Eqs. (6), (7) and (8), the inviscid radial and tangential momentum equations were integrated to yield

$$\Delta p = p - p_{\text{ref}} = \begin{cases} \dfrac{\rho}{2}\left(\dfrac{Qh}{\pi r_0^2}\right)^2\left(\dfrac{1}{4a^2}+S^2\right)\left(\dfrac{1}{r_{*\text{ref}}^2}-\dfrac{1}{r_*^2}\right), & 1 \leq r_*, \quad r_{*\text{ref}} > 1 \quad (11a) \\ \dfrac{\rho}{2}\left(\dfrac{Qh}{\pi r_0^2}\right)^2\left[-\left(\dfrac{r_*^2}{4a^2}+\dfrac{S^2}{r_*^2}\right)+\left(\dfrac{1}{4a^2}+S^2\right)\dfrac{1}{r_{*\text{ref}}^2}\right], & r_{c*} < r_* \leq 1, \quad (11b) \end{cases}$$

where

$$r_* = \frac{r}{r_0}. \tag{12}$$

Explicit account has been taken of the radial position (r_{ref}) at which the reference pressure is measured.

The quantity ($Qh/\pi r_0^2$) can be identified as a characteristic axial velocity V_{z0} through the updraft hole. Note that

$$V_{z0} = 2aV_{r0} \tag{13}$$

as expected from continuity.

The primary advantage of this simple model over others which contain only the tangential velocity component is that it incorporates some of the inertial effects due to the radial deceleration of the through flow. It explicitly recognizes the no-swirl limit (wherein $S \to 0$), in which the flow becomes analogous to that in a corner. In this case, defining v_r as in Eq. (6) and relating V_{r0} by means of the continuity equation as in Eq. (13) is appropriate. Further, Eq. (11) also includes the large swirl case ($2aS > 1$), but in this situation the simple model is expected to break down since there is no coupling between the tangential and flow-through fields. Greater care must be taken in identifying the characteristic radial and axial velocities, as a large portion of the flow in the convergence region tends toward cyclostrophic balance. As the flow approaches cyclostrophic balance (for very large values of $2aS$), it has been observed that the through-flow becomes progressively more confined to a thin end wall boundary layer and to the vortex core.

Using Eq. (11), several schemes to nondimensionalize the data can be formulated. To display the dependence of the profile or radial position in the confluence zone, Eq. (11a) indicates that the appropriate scaling is with a factor

$$\frac{\rho}{2}\left(\frac{Qh}{\pi r_0^2}\right)^2\left(\frac{1}{a^2}+4S^2\right).$$

In this case, for $r_* > 1$, all profiles should collapse to a single $1/r_*^2$-curve, with a nondimensional pressure deficit of

$$-\frac{1}{4}\left(1-\frac{1}{r_{*\text{ref}}^2}\right)$$

at $r_* = 1$. However, the region of primary interest is within the convergence zone ($0 \leq r_* \leq 1$); Eq. (11b) does not allow a simple, parameter-free scaling for this region. The best compromise was found to be a nondimensionalization such that

$$\Delta p_* = \frac{\Delta p}{\dfrac{\rho}{2}\left(\dfrac{Qh}{\pi r_0^2}\right)^2\dfrac{1}{a^2}}, \tag{14}$$

i.e., with respect to the characteristic radial velocity V_{r0}. The shapes of the profiles, at least for $r_{c*} < r_* \leq 1$ will then depend only on the ratio Γ/Q. A series of profiles, with each profile characterized by a different value of far-field circulation Γ, should then reveal the development of the whole vortex as a function of Γ/Q. While Eq. (11b) indicates that for the region $r_{c*} < r_* \leq 1$, the shape of the pressure deficit profile, when nondimensionalized as in Eq. (14), is independent of V_{r0}, one cannot extrapolate this finding into the core ($0 \leq r_* < r_{c*}$). Hence, it was found best to generate a series of families of profiles, each family being characterized by a different value of V_{r0}, to determine the dependence of the shape of the core-pressure profile and the magnitude of the central pressure drop on the swirl parameter.

Alternatively, if the updraft radius r_0, the total volume flow rate Qh and the ratio Γ/Q are held fixed, the right-hand side of Eq. (11), when nondimensionalized as in Eq. (14), is a parameter-free function. Thus, if the aspect ratio a is changed by varying the depth h (requiring that Γ be changed to maintain the ratio of Γ/Q), the profiles for $r_{0*} < r_*$ should collapse to one curve. Such profiles would then reveal the dependence of the pressure field in the central core on the aspect ratio.

5. Pressure profiles

Here are presented the radial profiles of wall static pressure as measured on the lower surface using the techniques described above. Discussion of these profiles focuses on events leading to the formation and progressive development of the swirling central core. The dependency of the profiles on r_*, where noted, was evaluated by plotting the profile in log-log coordinates, and determining the slope of the profile. Remarks on the accompanying velocity fields are based on observations of the visualized flow and limited hot-film anemometer data. Two cases chosen to illustrate the main features to be observed are examined first.

a. Profiles for no-swirl and for one- and two-celled vortices

Fig. 2 shows the nondimensional profiles of wall static pressure for a no-swirl flow, and for a flow at a moderate swirl ratio value ($S = 0.23$), the aspect ratio and the radial Reynolds number being the same in each case. The no-swirl profile shows that the greatest deficit occurred in the vicinity of $r_* = 1$, with the pressure deficit field in most of the confluence zone closely following an r_*^{-2} distribution. As the converging inflow neared the edge of the updraft hole, significant vertical motions developed, leading to the rounding off of the profile as $r_* \rightarrow 1$.

Across the convergence zone, the flow field resembled potential flow into a corner. This was reflected in the pressure profile as a broad region of slightly higher pressure, the highest value being at the centerline. The inflow thus encountered an adverse pressure gradient. In a loss-free flow, the resulting deceleration would be accomplished in such a manner that the pressure field would recover to its far-field value at the centerline. But since the adverse gradient here leads to separation of the lower surface boundary layer and turbulent losses of energy, the recovery was only partial. The centerline pressure was thus less than the far-field value. Separation occurred soon after the inflow had entered the convergence region, in the vicinity of $r_* \rightarrow 0.7$, so that the dimensionless central pressure deficit recovered only to -0.03. An internally recirculating stagnation region developed about the centerline.

With a swirl ratio of 0.23, the flow developed a cyclostrophic core which interacted with the lower surface. The vortex was characterized as being single-celled, with the axial velocity being everywhere upward and having a jetlike maximum about the axis.

The profile of Fig. 2 illustrates three key regions within the flow:

1) A region of nearly potential inflow across the confluence zone ($r_* > 1.0$) wherein both v_r and v_θ

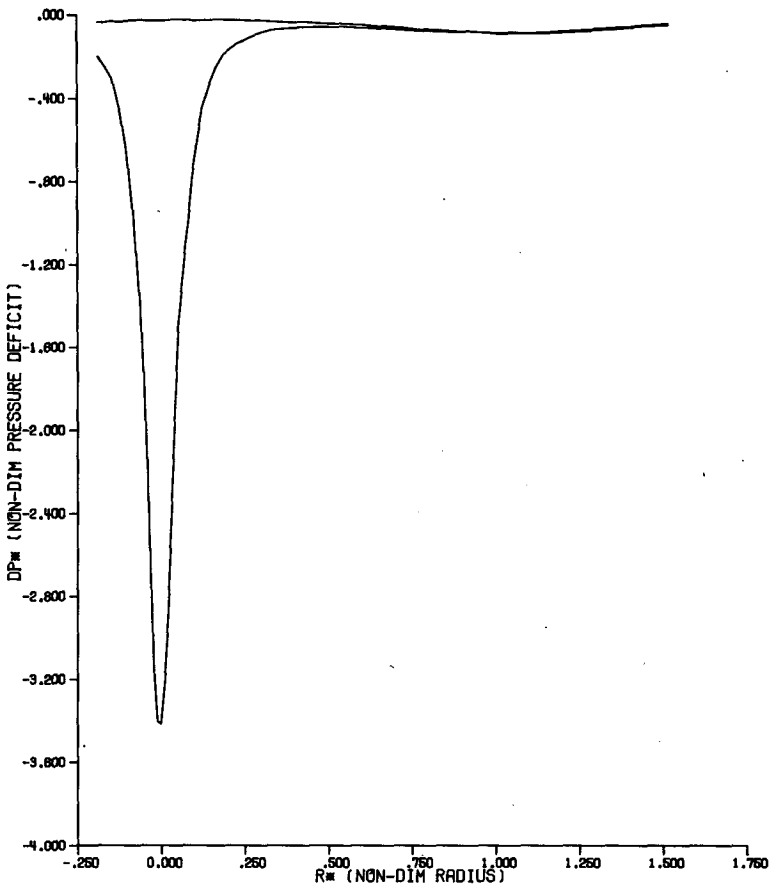

FIG. 2. Radial profiles of dimensionless wall static pressure measured on the lower surface beneath a no-swirl flow (upper curve) and beneath a single-celled vortex (lower curve): $a = 0.5$, $Re_r = 3.920 \times 10^5$ and (for the vortical flow) $S = 0.23$. Same profiles as a and c in Fig. 6.

were proportional to r_*^{-1}. As convergence of angular momentum had not yet produced serious modification to the stream surface, the pressure field closely resembled the no-swirl case.

2) A transition region across most of the convergence zone ($0.03 < r_* < 1.0$). This transition region consisted of an outer ring of higher pressure ($0.3 < r_* < 1.0$) and an inner region of pressure decreasing toward the axis ($0.03 < r_* < 0.3$). The high-pressure ring reflected the deceleration and upward turning of the meridional component of the flow, while in the inner region the conservation of angular momentum by the tangential component continued as the magnitude of the radial component decreased. This region provided a smooth transition between the rotational core and the irrotational far-field flow.

3) A small inner core region ($0 \leq r_* < 0.03$). The core radius of $r_{c*} \approx 0.03$ was evaluated by plotting the gradient of the pressure profile to determine the inflection point.

As the data plotted in Fig. 2 were obtained using a filtering procedure, they represent the mean pressure field. Vortex wander produced significant underestimation (by 20–40%) of the maximum deficit and the abrupt flattening of the core near the central axis. The importance of this effect decreased rapidly with increasing radius, with data for $r_* \geq 0.05$ being essentially uncontaminated. Instantaneous observations made by viewing the output of the transducer on an oscilloscope indicated that the true maximum central pressure deficit was in the range $-4.0 > \Delta p_* > -5.0$.

A pressure profile across a radically different core structure is shown in Fig. 3. For this very high swirl ratio flow ($S = 1.63$), the structure was that of a two-celled vortex, consisting of an outer irrotational flow surrounding an annulus of high-velocity spiraling upflow. Within the annulus was vertically recirculating core flow. Downflow occurred along the axis, surrounded by a weak return (up) flow merging into the main upflow. The pressure field outside the core was found to be $\propto r_*^{-2}$ all the way in through the confluence zone and in the outer convergence zone. The region of potential flow terminated abruptly—no solidly rotating core was

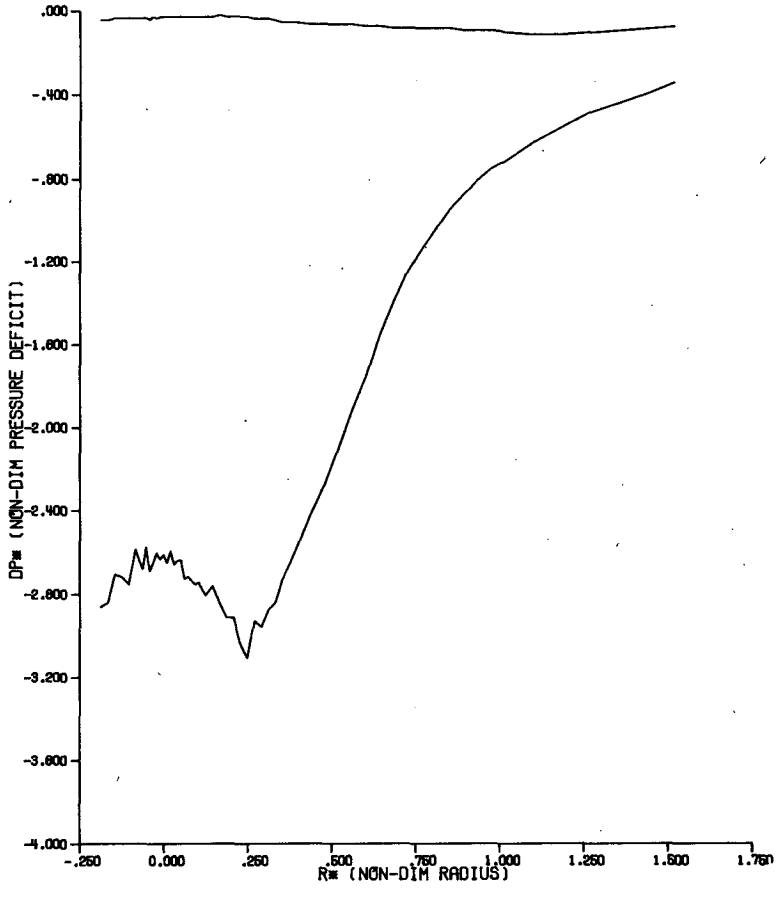

FIG. 3. Radial profiles of dimensionless wall static pressure measured on the lower surface beneath a no-swirl flow (upper curve) and beneath a two-celled vortex (lower curve): $a = 0.5$, $\mathrm{Re}_r = 1.507 \times 10^5$ and (for the vortical flow) $S = 1.79$. Same profiles as a and g in Fig. 4.

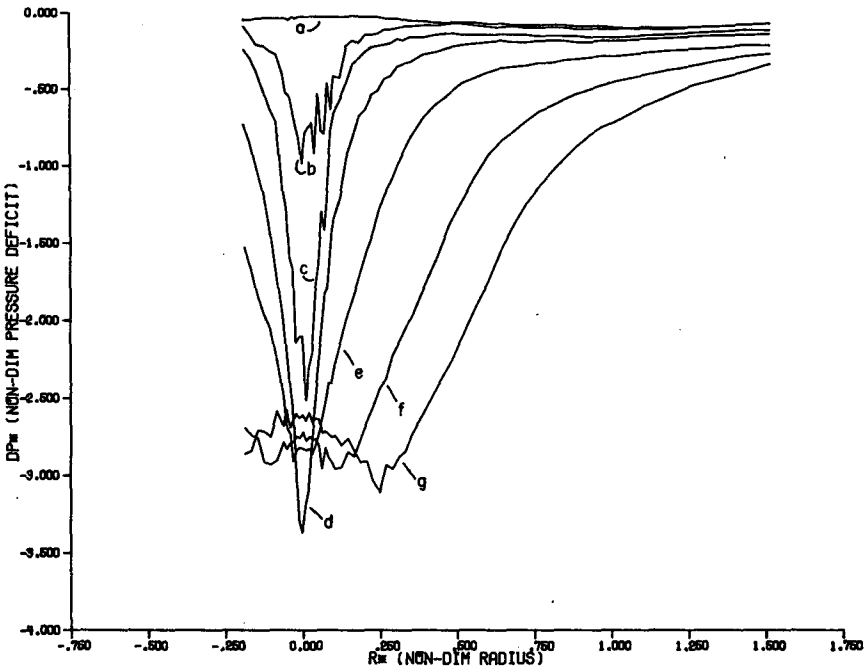

FIG. 4. A family of dimensionless wall static pressure profiles measured on the lower surface for the conditions noted in Table 1.

present. Rather, a ring of lowest pressure divided the outer flow from that within the core. Flow visualization revealed that this was beneath the annulus of spiraling upflow. A key feature to note in Fig. 3 is the central pressure rise contained within the ring of lowest pressure. This is interpreted as being due to the deceleration of the downflow coming in from above this region. Such a dynamic high has been previously predicted by Rotunno (1977) via a numerical model.

This form of vortex is usually accompanied by a pattern of two or more subsidiary vortices that develop in the zone of strong shear at the outer edge of the core. Since the measurements were taken

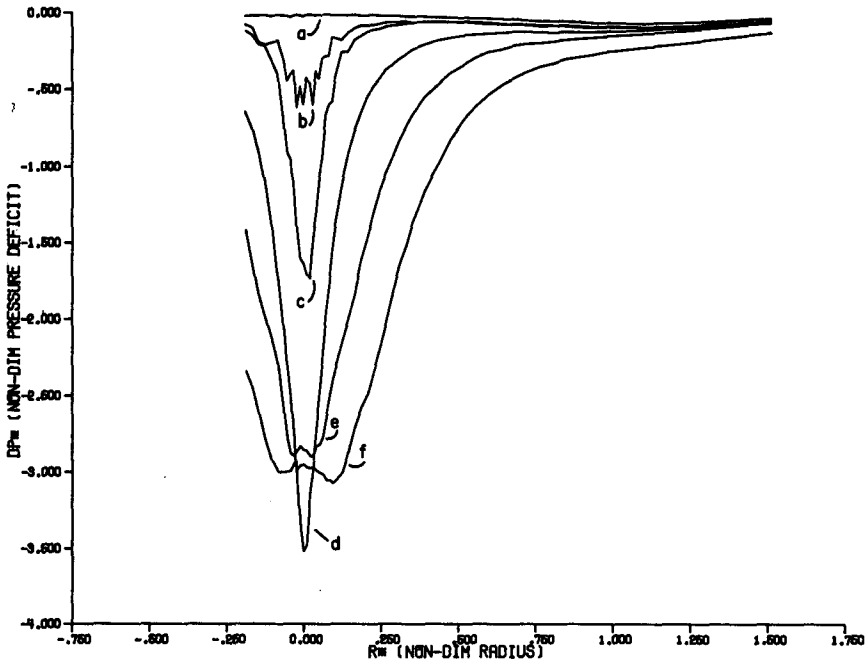

FIG. 5. As in Fig. 4 except for the conditions noted in Table 2.

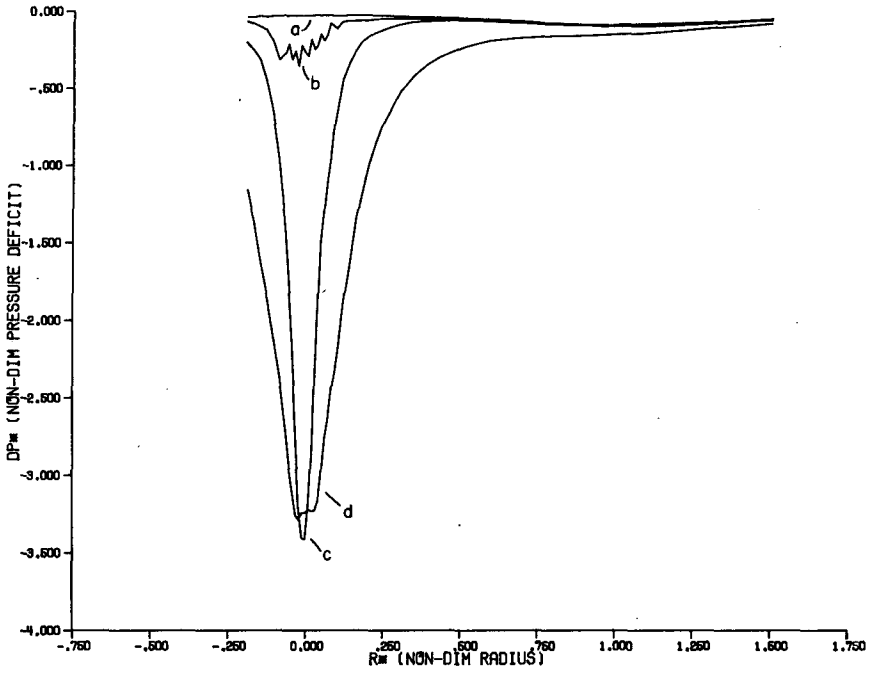

FIG. 6. As in Fig. 4 except for the conditions noted in Table 3.

using a long time constant first-order filter, the high-frequency fluctuations due to the subsidiary vortices were filtered out. Also, since the core region is broad and free from wander, the qualification on the validity of the central-core region pressure values made above does not apply.

b. *The pressure field as a function of swirl ratio*

The three families of dimensionless pressure profiles shown in Figs. 4–6 illustrate the development of the surface pressure profile as a function of swirl ratio. The values of the dimensionless parameters for each individual curve are listed in Tables 1–3. Note that the updraft radius and the inflow depth were held constant at 30.48 and 60.96 cm, respectively, fixing the internal aspect ratio at 0.50. Within each family, the volume flow rate Qh (hence the radial Reynolds number Re_r) was held fixed to within $\pm 1\%$. To produce each family, the screen speed Ω_s was varied incrementally to change the swirl ratio between determinations of the profiles. The nondimensionalization scheme of Eq. (14) was used. Each family thus shows the response of the surface mean pressure field to a progressive increase in swirl parameter at specified Re_r and a. That is, they each illustrate the progressive development of the flow from a no-swirl situation to a single-celled vortex to a two-celled vortex as the input swirl is increased. With the aspect ratio fixed, intercomparison of the three families gives some indication of the response to variations in Re_r.

In each family, the curve a profile presents the no-swirl situation. These each show a broad

TABLE 1. Conditions used to produce the curves in Fig. 4.

Curve	S	a	Γ/Q	Re_r	θ (deg)	Qh ($\mathrm{m^3\ s^{-1}}$)	Ω_s ($\mathrm{rad\ s^{-1}}$)
a*	—	0.5	—	1.498×10^5	2.25	0.662	0.000
b	0.14	0.5	0.14	1.498×10^5	8.00	0.662	0.029
c	0.29	0.5	0.29	1.499×10^5	16.25	0.662	0.060
d	0.42	0.5	0.42	1.515×10^5	22.74	0.669	0.093
e	0.60	0.5	0.60	1.508×10^5	31.02	0.666	0.158
f	1.17	0.5	1.17	1.498×10^5	49.48	0.662	0.265
g	1.79	0.5	1.79	1.507×10^5	60.87	0.666	0.356

* Note: A Θ value is reported for curve a even though this was a no-swirl situation made without screen rotation. In combination with similar values in Table 2 and 3, this gives an indication of the accuracy to which the inflow angle θ can be measured by the technique described in Church *et al.* (1979).

TABLE 2. Conditions used to produce the curves in Fig. 5.

Curve	S	a	Γ/Q	Re_r	θ (deg)	Qh ($m^3 s^{-1}$)	Ω_s (rad s^{-1})
a*	—	0.5	—	2.454×10^5	1.98	1.084	0.000
b	0.08	0.5	0.08	2.465×10^5	4.60	1.089	0.030
c	0.14	0.5	0.14	2.442×10^5	7.93	1.079	0.059
d	0.35	0.5	0.35	2.444×10^5	19.10	1.080	0.157
e	0.52	0.5	0.52	2.439×10^5	27.59	1.078	0.263
f	0.82	0.5	0.82	2.428×10^5	39.27	1.073	0.359

* See note 1 on Table 1.

central region of slightly higher pressure, with the lowest pressure in a circular trough beneath the lip of the updraft hole. As noted previously, such a profile resulted in boundary-layer separation in the outer portion of the convergence zone. This gave rise to a large stagnation region consisting of a shallow layer over the lower surface and an upright cone-shaped region around the central axis.

For small swirl ratio values (curve b), a weakly swirling flow *without* a central core was obtained. It was in this formative stage that the outer high-pressure ring first appeared. Since for small swirl, the magnitude of the inverse gradient presented by this ring of higher pressure to the inflow was still sufficient to trigger boundary-layer separation, air with significant angular momentum was prevented from approaching near the axis at low levels. The initial development of the central pressure well was a response to the development of a core zone well aloft. *As a direct consequence of the stagnation region at surface, for these conditions (fixed Q and a), the vortex built downward from above with increasing swirl, rather than upward from surface.*

As Ω_s was incrementally increased, the ring of high pressure was eroded from the inside out (its outer circumference is fixed by the geometry of the apparatus). As the input swirl was increased, the dynamic pressure deficit induced by the intensifying swirling flow aloft offset the pressure rise due to the decelerating radial component. The greatest induced pressures were in the vicinity of the axis, so that the central pressure well deepened and gradually widened.

Initially, the favorable gradient presented to the inflow by the deepening central pressure well caused the center of the stagnation region to thin out. Eventually, a point (typically $S \approx 0.10$) was reached where the central pressure well presented such a strong favorable gradient that the separated inflow was forced to reattach to the lower surface at some radius inside the line of separation. A small but intense central core in contact with the lower surface formed as the reattached fluid accelerated into close proximity of the central axis. The visualized high-pressure ring then corresponded to a ring-shaped stagnation region in the outer portion of the convergence zone. Further increases in input swirl reduce both the vertical thickness and radial width of this ring. At about $S \approx 0.20$ the component of the pressure field induced by the increased convergence of angular momentum strengthened to where it prevented boundary-layer separation altogether; fluid flowed directly from the confluence region into the core via a thin, accelerating boundary layer. At this point a well-developed single-celled vortex extended to the lower surface.

For $0.1 \leqslant S \leqslant 0.5$, a series of vortex breakdowns progressively developed in the core in the convection region and moved upstream with increasing swirl. By $S \approx 0.5$, these had all reached the lower surface and the flow had become two-celled. In response to these developments, the central portion of the pressure profile first flattened out (curve e in Figs. 3 and 4 and curve d in Fig. 6), and with further increases in swirl ratio, began to reflect the small, central high discussed previously (profile f in Figs. 3 and 4). For very large swirl ($S \geqslant 1.0$), the inner core contained a well-developed central high (profile g in Fig. 3), with the lowest mean pressures being found in an annular ring at the edge of the core. During the development state ($0.5 < S < 1.0$), the central pressure rose in the core, but for very large swirl

TABLE 3. Conditions used to produce the curves in Fig. 6.

Curve	S	a	Γ/Q	Re_r	θ (deg)	Qh ($m^3 s^{-1}$)	Ω_s (rad s^{-1})
a*	—	0.5	—	3.913×10^5	−0.37	1.73	0.000
b	0.08	0.5	0.08	3.917×10^5	4.76	1.73	0.030
c	0.23	0.5	0.23	3.920×10^5	13.13	1.73	0.156
d	0.47	0.5	0.47	3.917×10^5	25.32	1.73	3.61

* See note 1 on Table 1.

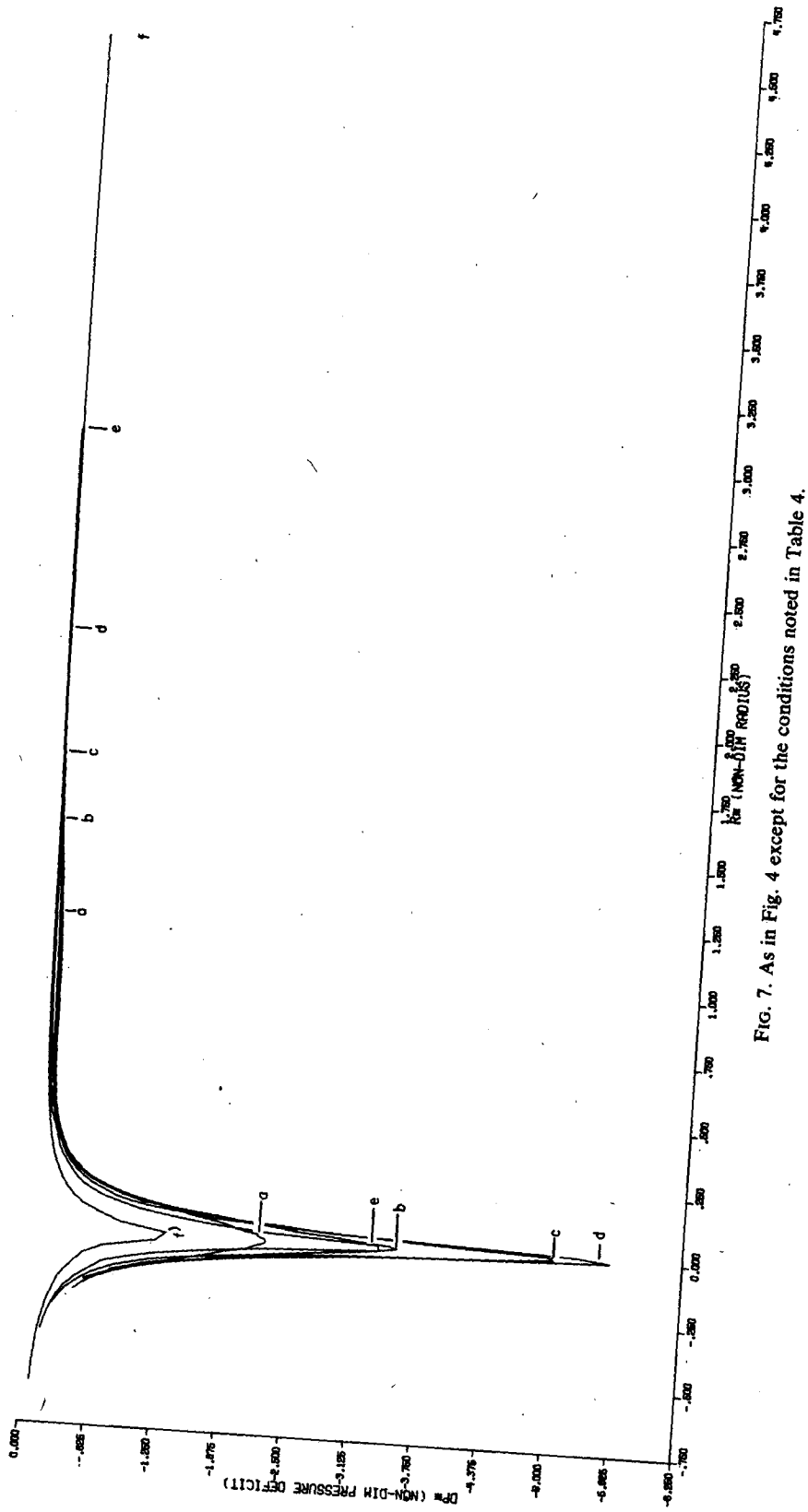

FIG. 7. As in Fig. 4 except for the conditions noted in Table 4.

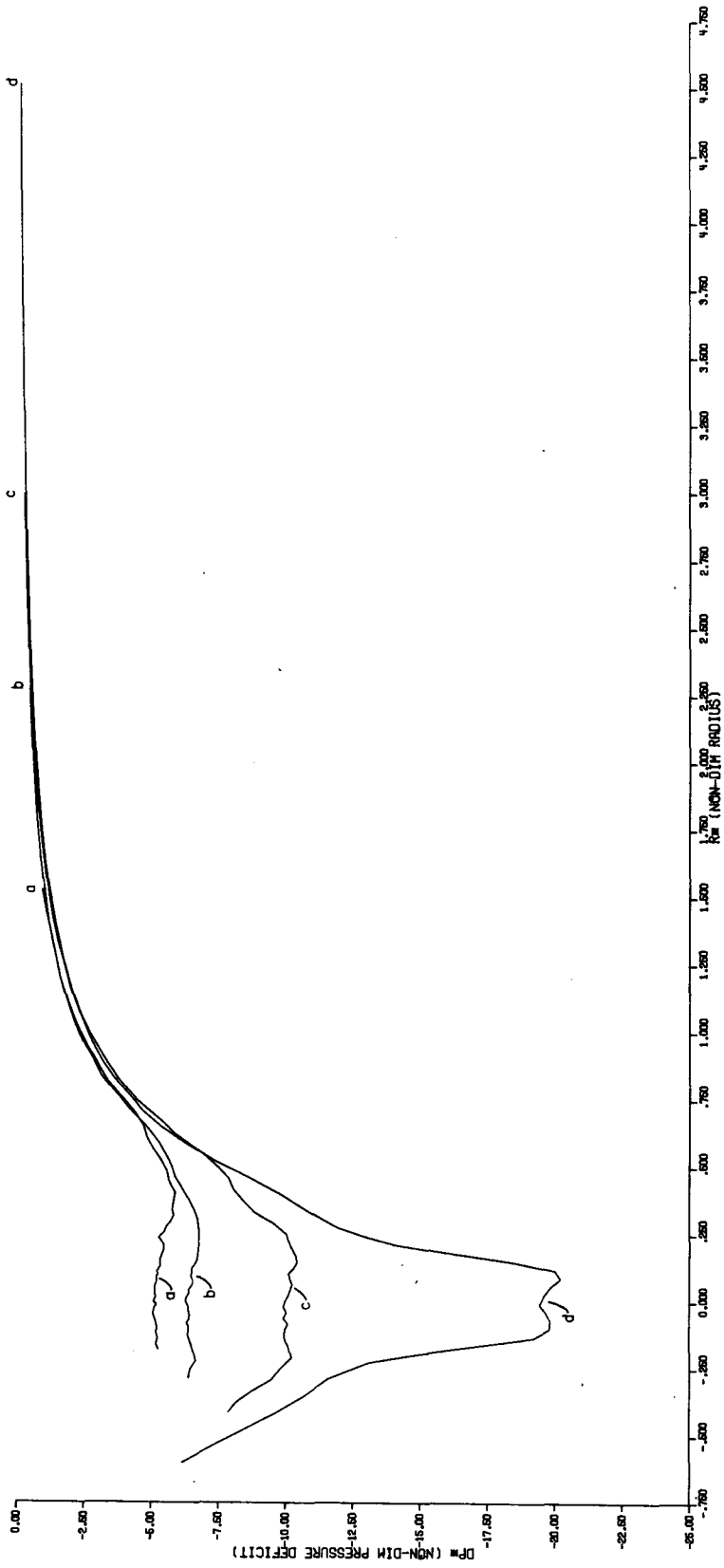

FIG. 8. As in Fig. 4 except for the conditions noted in Table 5.

TABLE 4. Conditions used to produce the curves in Fig. 7.

Curve	S	a	Γ/Q	Re_r	θ (deg)	Qh ($m^3 s^{-1}$)	Ω_s (rad s^{-1})
a	0.45	0.38	0.35	2.466×10^5	19.14	1.090	0.154
b	0.33	0.5	0.33	2.464×10^5	18.52	1.089	0.153
c	0.29	0.6	0.34	2.468×10^5	18.88	1.091	0.156
d	0.23	0.75	0.34	2.492×10^5	18.91	1.101	0.155
e	0.17	1.0	0.35	2.390×10^5	19.28	1.056	0.155
f	0.12	1.5	0.36	2.458×10^5	19.56	1.086	0.155

values, the mean pressures in the central zone began to gradually fall once more. The core broadened out significantly.

c. Dependence on aspect ratio

To determine the role played by the internal aspect ratio, two additional families of profiles were investigated. These are shown in Figs. 7 and 8, where the nondimensionalization is by Eq. (14). A different volume flow rate was used in each family. The swirl parameter and the inflow depth h were held fixed in each family, while the radius of the updraft hole was varied. By Eq. (11), when nondimensionalized in the manner stated, it is expected that the profiles will all fall on the same curve for $r_{c^*} < r_*$. The data have been found to agree reasonably well with this prediction.

Recognizing the shapes of the profiles in Fig. 7 to be generally indicative of one-celled vortices, this family of curves shows the variation of the dimensional core pressure deficit with increasing aspect ratio/decreasing swirl ratio to have been a $\rightarrow$ b $\rightarrow$ c $\rightarrow$ d $\rightarrow$ e $\rightarrow$ f. As the aspect ratio was increased, the vortex core changed from one in which the vertical velocity was off-axis (profile a) to one with no concentrated core (profile f). Fig. 8 shows the corresponding progression that occurred in what were identified as two-celled vortices. In Fig. 8, profile a represents the pressure field beneath a large two-celled flow of large swirl ratio (small aspect ratio); profile d was also two-celled, but for a smaller value of swirl ratio (larger aspect ratio).

d. Variations in the central pressure

As a result of the complex behavior indicated by Figs. 4–8, the surface pressure deficit at the center of a vortex was measured (without filtering) while the screen rotation rate was varied, all other parameters being held fixed. The resulting plot of dimensionless central-pressure deficit versus swirl ratio is shown in Fig. 9. Consistent with previous findings, this indicated four distinct regimes of flow:

1) Region A in Fig. 9 is characterized by a moderate decrease in central pressure as swirl ratio increases. Visual observation of the surface flow showed it was controlled by separation of the inflow at large radius. A concentrated core existed aloft, but did not extend downward to the surface.

2) In region B, entered as the swirl ratio increased beyond $S \approx 0.15$, the central pressure increased slightly. Flow visualization suggested that the favorable external pressure gradient imposed on the separated surface boundary layer had become strong enough to force reattachment. A small laminar core was in contact with the surface at the centerline. An annular region of internally recirculating fluid was visible in the outer portion of the convergence zone for $0.15 \leqslant S \leqslant 0.22$. As S was slowly increased, this smoke-filled ring flattened, eroded from the inside outward and disappeared at $S \approx 0.22$.

3) With $S \geqslant 0.22$, the full concentrated vortex core penetrated to surface. The great pressure fall characterizing region C represented the progressive intensification of this single-celled vortex core. The innermost core flow throughout this stage appeared to remain laminar.

4) The left-hand boundary of region D ($S \approx 0.42$) in Fig. 9 corresponded to the onset of turbulence within the core coincident with the penetration of a vortex breakdown to surface. From this point on, as S increased, the core expanded rapidly with downflow developing along the axis. The rise in central pressure as S becomes large reflected the in-

TABLE 5. Conditions used to produce the curves in Fig. 8.

Curve	S	a	Γ/Q	Re_r	Θ (deg)	Qh ($m^3 s^{-1}$)	Ω_s (rad s^{-1})
a	4.28	0.5	4.28	9.047×10^4	76.85	0.340	0.359
b	2.63	0.75	3.94	9.382×10^4	75.75	0.415	0.355
c	2.32	1.0	4.64	8.474×10^4	77.83	0.374	0.349
d	1.61	1.5	4.82	8.910×10^4	78.27	0.394	0.363

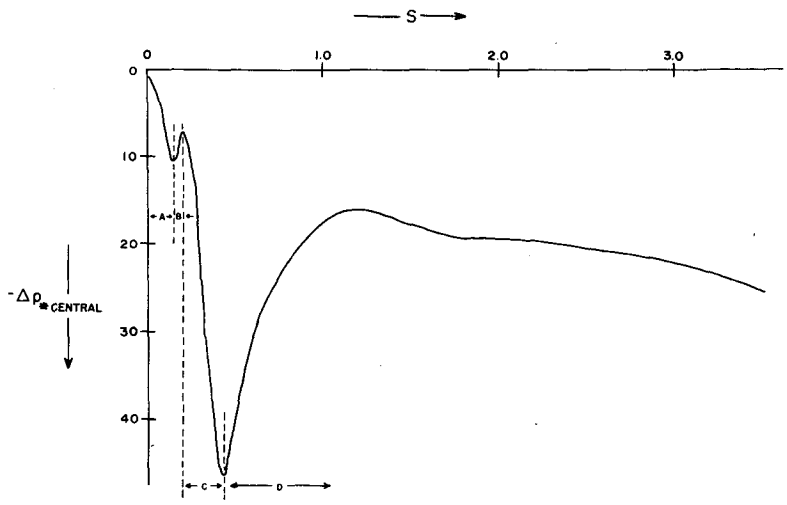

FIG. 9. Plot of dimensionless central pressure versus swirl ratio for $a = 0.6$ and $Re_r = 1.87 \times 10^5$. The curve indicates the unfiltered maximum as observed on an oscilloscope.

tensification of the central downdraft and the loss of a concentrated central core. For very large S, the strong centrifugal force field prevented significant convergence from taking place. Up to $S \approx 0.42$, the plot of central pressure is also a plot of maximum pressure deficit. In region D, the lowest pressure was off-axis in an annular ring.

6. Summary and conclusions

The data presented herein allow one to draw a picture of the structure of the surface pressure field as determined by the primary internal dimensionless parameters S, Re_r and a. It has been found that the surface pressure field in the convergence region outside the central core is determined by two processes:

- Radial inertial forces acting to decelerate the inflow by establishing a region of higher pressure about the centerline. The resulting pressure gradient varies as $-r^{+1}$, and has a maximum in the outer portion of the convergence zone whose magnitude appears to be proportional to r_0^{-2}. The presence of the resulting adverse gradient triggers separation of the surface boundary layer.
- The dynamic pressure field induced by the conservation of angular momentum acting to produce a region of lower pressure about the centerline. The resulting gradient varies approximately as $+r^{-3}$ and has a maximum near the vortex core radius whose magnitude appears to be proportional to r_0^{+2} and r_c^{-3}. The resulting favorable gradient works to accelerate fluid in the surface boundary layer.

The component of the pressure induced by the conservation of angular momentum can thus be seen to act to offset that due to inertial effects, and, as swirl increases, to force reattachment of the separated boundary layer and to eventually prevent separation altogether. From this, one can now recognize both the cause of, and the role played by, the outer pressure ring (humps) observed in microbarograph traces obtained in the vicinity of some tornadoes.

Further, the data show the strong influence exerted by the development and upstream propagation of vortex breakdowns in the core. These lead to the evolution from a single-celled vortex to a two-celled one. Somewhat surprisingly, the largest (mean field) central-pressure deficits were found in single-celled vortices characterized by intermediate swirl ratio values. With the development of the two-celled structure, the lowest pressures were found off-axis in an annular region. These remained relatively constant, or even rose as swirl was increased further. Only at the very highest swirl ratios did they start to slowly decrease again. Clear quantitative evidence (in the form of a central dynamic high) for the existence of a core downdraft has been presented. This is substantiated by observations of the visualized flow.

Based on the above, it is felt that this initial objective of modeling the mean pressure field of a tornado cyclone system has been successful in replicating the natural event. The results provide a great deal of insight into vortex dynamics and should be useful in interpreting microbarograph traces. Future work will focus on investigation of the time-dependent pressure fields associated with the multiple vortices that occur embedded within the large two-celled flows.

Acknowledgments. The authors wish to acknowledge Ms. Gene Shelley and Ms. Sharon Von Tobel for their assistance in technical typing and in preparation of the manuscript, and Mr. Randal Pauley for his assistance in preparation of the manuscript. This work was supported by the National Science Foundation under Grant ATM 77-16955.

REFERENCES

Church, C. R., J. T. Snow and E. M. Agee, 1977: Tornado vortex simulation at Purdue University. *Bull. Amer. Meteor. Soc.*, **58,** 900–908, cover photo.

——, ——, G. L. Baker and E. M. Agee, 1979: Characteristics of tornado-like vortices as a function of swirl ratio: A laboratory investigation. *J. Atmos. Sci.*, **36,** 1755–1776.

Davies-Jones, R. P., 1973: The dependence of core radius on swirl ratio in a tornado simulator. *J. Atmos. Sci.*, **30,** 1427–1430.

——, 1976: Laboratory simulations of tornadoes. *Proc. Symp. on Tornadoes*. Lubbock, Dept. of Civil Engr., Texas Tech University, 151–173.

Fujita, T. T., 1959: A detailed analysis of the Fargo tornadoes of June 20, 1957. Tech. Rep. No. 5, Severe Local Storms Project, University of Chicago, 129 pp.

——, 1970: The Lubbock tornadoes: A study of suction spots. *Weatherwise*, **23,** 161–173.

Lewellen, W. S., 1962: A solution for three-dimensional vortex flows with strong circulation. *J. Fluid. Mech.*, **14,** 420–432.

Rotunno, R., 1977: Numerical simulation of a laboratory vortex. *J. Atmos. Sci.*, **34,** 1942–1956.

Ward, N. B., 1964: The Newton, Kansas tornado cyclone of May 24, 1962. *Preprints Eleventh Weather Rader Conf.*, Boulder, Amer. Meteor. Soc., 410–415.

——, 1972: The exploration of certain features of tornado dynamics using a laboratory model. *J. Atmos. Sci.*, **29,** 1194–1204.